



**HAL**  
open science

## Processing of highly porous bioglass monoliths by hydrothermal hot pressing

B. Degraeve, B. Lefevre, N. Rocton, N. Herbert, N. Hamrouni, Grégory Hauss, Alain Largeteau, Mythili Prakasam, Hassane Oudadesse, Odile Merdrignac-Conanec

► **To cite this version:**

B. Degraeve, B. Lefevre, N. Rocton, N. Herbert, N. Hamrouni, et al.. Processing of highly porous bioglass monoliths by hydrothermal hot pressing. *Ceramics International*, 2022, 48 (13), pp.18190-18198. 10.1016/j.ceramint.2022.03.078 . hal-03643101

**HAL Id: hal-03643101**

**<https://univ-rennes.hal.science/hal-03643101>**

Submitted on 1 Jun 2022

**HAL** is a multi-disciplinary open access archive for the deposit and dissemination of scientific research documents, whether they are published or not. The documents may come from teaching and research institutions in France or abroad, or from public or private research centers.

L'archive ouverte pluridisciplinaire **HAL**, est destinée au dépôt et à la diffusion de documents scientifiques de niveau recherche, publiés ou non, émanant des établissements d'enseignement et de recherche français ou étrangers, des laboratoires publics ou privés.

## Processing of highly porous bioglass monoliths by hydrothermal hot pressing

B. Degraeve<sup>a</sup>, B. Lefevre<sup>a</sup>, N. Rocton<sup>a</sup>, N. Herbert<sup>a</sup>, N. Hamrouni<sup>a</sup>, G. Hauss<sup>b</sup>, A. Largeteau<sup>c</sup>, M. Prakasam<sup>c</sup>, H. Oudadesse<sup>a</sup>, O. Merdrignac-Conanec<sup>a</sup>

<sup>a</sup>Univ Rennes, CNRS, ISCR UMR 6226, 35042, Rennes, France

<sup>b</sup>Univ. Bordeaux, CNRS, PLACAMAT, UMS 3626, F-33600 Pessac, France

<sup>c</sup>Univ. Bordeaux, CNRS, Bordeaux INP, ICMCB, UMR 5026, F-33600 Pessac, France

### Abstract

Porous bioglass monoliths have been processed by hydrothermal hot pressing (HyHP) from sol-gel and melt-derived bioglass powders of composition (in mol %): SiO<sub>2</sub>-CaO-P<sub>2</sub>O<sub>5</sub> (55.0-40.0-5.0) and SiO<sub>2</sub>-CaO-Na<sub>2</sub>O-P<sub>2</sub>O<sub>5</sub> (47.2-26.4-23.8-2.6), respectively. An open porosity of >70% ever reached in 3D structures is reported for monoliths issued from sol-gel powders. Dissolution studies were performed in simulated body fluid (SBF) for 1-30 days. The monoliths were analysed using XRD, FTIR and SEM to observe the formation of an apatite-like layer and elemental concentration of SBF was evaluated using ICP/OES analysis. A higher kinetics in the development of apatite layer was observed for sol-gel derived monoliths. This result is explained by the high surface areas of the nanosized sol-gel powders and the possibility of HyHP to create large porosity (mesoporous monoliths) and retain large surface areas. HyHP is also effective in processing 3D-bioglass structures with porosity gradient by co-sintering powders of different size.

**Keywords** : highly porous monolith, hydrothermal hot pressing, sol-gel derived bioglass, melt-derived bioglass, sintering

### Introduction

Recent developments in processing methods of bioactive glasses for bone regeneration focus on porous scaffolds that can act as three-dimensional (3D) templates to mimic the bone structure. Besides conventional foaming techniques and template-based methods, various additive manufacturing (or solid freeform fabrication) methods are now available for building scaffolds from both melt- and sol-gel-derived glasses while offering over aforementioned techniques a better control of scaffold architecture and pore morphology [1,2]. Nevertheless, a final thermal treatment (usually up to 550-700°C) has to be performed to burn out the binders or templating agents and sinter the glass powders. This final step is critical as it may provoke glass devitrification while complete organics removal is recommended [1,2]. Hydrothermal processes, formerly investigated for the preparation of  $\alpha$ -quartz single crystal for its unique piezoelectric properties, are now widely developed for the preparation of new materials and grow bulk crystals for specific applications [3]. Owing to its similarity to natural bone

1  
2  
3  
4  
5  
6  
7  
8  
9  
10  
11  
12  
13  
14  
15  
16  
17  
18  
19  
20  
in chemical composition, hydroxyapatite (HA,  $\text{Ca}_{10}(\text{PO}_4)_6(\text{OH})_2$ ) has become an excellent biomaterial for bone repair and is currently fabricated into scaffolds [4–6]. Yamazaki *et al.* developed first the concept of the sintering by hot-pressing under hydrothermal conditions for the preparation of strong porous hydroxyapatite (HA) ceramics with 42% open porosity after 3h-post-sintering at 1050°C [7]. Nakahira *et al.* reported also a hydrothermal hot pressing method followed by a post-sintering at 1100°C to fabricate porous hydroxyapatites with high strength and about 40% open porosity [8]. However, hydrothermal processes have been scarcely reported for the production of porous bioactive glasses. Yet, the latter could take advantage of the opportunities of hydrothermal process such as one-step sintering procedure and low reaction temperatures (<375°C). To our knowledge, hydrothermal hot-pressing (HyHP) investigated on glass materials is only reported so far for the preparation of porous glass compacts to develop an alternative route for the recycling of used glasses (TV panel glass) for environmental concerns [9,10]. In this process, porous compacts produced by heating at 750°C the compacts densified by HyHP had a large amount of closed pores (58%).

21  
22  
23  
24  
25  
26  
27  
28  
29  
30  
31  
32  
33  
34  
35  
36  
37  
38  
39  
40  
41  
42  
43  
44  
45  
46  
47  
48  
49  
50  
51  
52  
53  
54  
55  
56  
57  
58  
59  
60  
61  
62  
63  
64  
65  
The objective of this research is to produce porous bioactive monoliths from bioglass powders using the low temperature HyHP technique. The motivation is quintuple (i) to retain the amorphicity of the solid giving rise to a high reactivity in physiological fluids i.e. the ability to form *in situ* a hydroxyapatite layer on its surface [11,12] (ii) to avoid grains growth so that to enhance the specific surface area and porosity of the final biomaterial to accelerate the kinetics of the formation of HA layer [13] (iii) to produce open porosities and interconnected structures that are essential for cell nutrition, proliferation, and migration for tissue vascularization and formation of new tissues [14] (iv) to limit the loss of thermosensitive molecules such as  $\text{H}_2\text{O}$ , -OH groups, present in the precursor and (v) to make possible the functionalization of their surface with thermosensitive therapeutic agents (molecules of biological interest). The technique was applied to bioglass powders synthesized by sol-gel and melt quenching methods. The aim of the study is not to compare the two bioglasses but to find a process that allows to produce monoliths with high porosity and good mechanical strength. The study investigated sol-gel derived bioglass nanopowders in the  $\text{SiO}_2$ -CaO- $\text{P}_2\text{O}_5$  ternary system referred as NBG of composition : (in mol %)  $\text{SiO}_2$ -CaO- $\text{P}_2\text{O}_5$  (55.0-40.0-5.0) and melt-derived bioglass powders, termed as BG, of composition: (in mol %)  $\text{SiO}_2$ -CaO- $\text{Na}_2\text{O}$ - $\text{P}_2\text{O}_5$  (47.2-26.4-23.8-2.6) which have been the subject of various studies within our laboratory proving a high potential for applications on the biomedical field [15–20]. Let us note that the NBG sol-gel composition does not require  $\text{Na}_2\text{O}$  where in melt-quenched BG the primary role of  $\text{Na}_2\text{O}$  is to lower the melting point, improving processability. The bioactivity of the monoliths was evaluated by examining the ability of apatite to form on their surface by *in vitro* procedure involving the glass dissolution and its time-dependency in simulated body fluid (SBF) [21]. Our original HyHP process technique is first reported to produce highly porous bioglass-based monoliths ( $p > 50\%$ ).

## 1. Experimental

### 1.1. Bioglass nanopowder synthesis

Sol-gel derived NBG powder samples were prepared according to the following procedure issued from previous work [17]. Tetraethyl orthosilicate or TEOS ( $\text{Si}(\text{OC}_2\text{H}_5)_4$ ) (99%, Merck), sodium trimetaphosphate ( $\text{Na}_3\text{P}_3\text{O}_9$ ) (95%, Alfa Aesar) and calcium nitrate tetrahydrate  $\text{Ca}(\text{NO}_3)_2 \cdot 4\text{H}_2\text{O}$  (98%, Fluka) were used as silica, phosphorous and calcium sources, respectively. The experimental protocol is based on the preparation and the mixture of two different emulsions, A and B. Triton X-100® (99%, Alfa Aesar) and octanol (99%, Alfa Aesar) were used as surfactants and cyclohexane (100%, VWR) was used as oil phase for the preparation of both emulsions. Emulsion A was prepared by dissolution in a 2.5M aqueous ammonia solution, under magnetic stirring of appropriate amounts of TEOS and  $\text{Na}_3\text{P}_3\text{O}_9$ . This mixture was kept under strong agitation for one hour to allow the TEOS hydrolysis. Emulsion B is an aqueous solution of appropriate amount of  $\text{Ca}(\text{NO}_3)_2 \cdot 4\text{H}_2\text{O}$ . The two emulsions A and B were subsequently mixed at a constant and vigorous speed for one hour to mix the reagents contained in the aqueous reactors of the emulsions. The mixed emulsions were then left to rest for a maturation (polymerization) time of less than 1 hour. After maturation, a white gel is collected by centrifugation and washed several times with ethanol to remove most of the surfactants and dried overnight at 100°C in an oven. The resulting white powder is calcined in air at 620°C for 4 hours in a muffle furnace and subsequently mechanically ground in water. After centrifugation, washing with ethanol and drying in an oven at 80 °C under vacuum, the obtained powder is of nanometric size (< 100 nm). Chemical analysis (ICP-OES) revealed that no sodium impurity was present after the preparation steps.

The melt-derived BG glass was prepared by reacting appropriate amounts of calcium metasilicate  $\text{CaSiO}_3$  (99%, Alfa Aesar), sodium metasilicate  $\text{Na}_2\text{SiO}_3 \cdot 5\text{H}_2\text{O}$  (99.5%, Fischer) and sodium trimetaphosphate ( $\text{Na}_3\text{P}_3\text{O}_9$ ) (95%, Alfa Aesar) according to the experimental procedure described in our previous work [16]. The resulting glass was crushed and sieved to select two different particle sizes: 40-63  $\mu\text{m}$  (coarse BG) and < 40  $\mu\text{m}$  (fine BG).

### 1.2. Elaboration of the monoliths by HyHP

The HyHP process (Fig.1) is applied inside a hydrothermal autoclave with 10 mm internal diameter. (detailed information in [22,23]). Table 1 reports the HyHP sintering parameters (temperature (°C), external applied force (kN), holding time (min) and nature/quantity of the solvent) selected in order to form compacts with good mechanical strength. Initial tests showed that a minimum force of 0.5 kN was required to obtain well-sintered pellets and that it was necessary to operate below 200°C and limit the amount of solvent added (either deionized  $\text{H}_2\text{O}$  or NaOH-2M aqueous solution) to prevent crystallization. It was also found that, for BG powders, hydrothermal sintering must be realized in NaOH-2M to obtain well-sintered BG pellets. We therefore chose to operate, for both powders, at a temperature of 150°C with an external force of 0.5 kN in presence of 80 to 240  $\mu\text{L}$  of solvent. The highest solvent ratio was determined to ensure that solvent surrounds the bioglass particles uniformly

so that they are concerned by the hydrothermal sintering and avoid both the formation of a paste before pressing and exudation during the sintering. The hydrothermal pressure generated by the solvent is lower than the pressure exerted at bioglass intergranular contacts by the hot-press (0.5kN = 64bar).

Table 1  
Parameters of HyHP applied on NBG and BG powders (0.2g powder, 10mm diameter) and thickness of monoliths after HyHP.

Sample	Time (min)	Solvent	Vol ( $\mu\text{L}$ )	T ( $^{\circ}\text{C}$ )	F (kN)	Thickness (mm)
<b>NBG</b>						
NBG-231	30	NaOH-2M	80	150	0.5	3.37
NBG-232	30	H <sub>2</sub> O	80	150	0.5	3.71
NBG-255	5	no	no	150	0.5	3.6
NBG-256	5	NaOH-2M	80	150	0.5	3.6
NBG-257	5	H <sub>2</sub> O	80	150	0.5	3.61
NBG-259	5	NaOH-2M	160	150	0.5	3.7
NBG-260	5	NaOH-2M	240	150	0.5	3.37
NBG-261	5	NaOH-2M	240	100	0.5	3.27
<b>Coarse BG</b>						
BG-264	5	NaOH-2M	60	150	0.5	1.7
<b>Fine BG</b>						
BG-229	5	NaOH-2M	80	150	0.5	1.71

The samples were very strong even at short sintering time (5 min) showing the benefit of hydrothermal conditions on sintering. The quality of the pellets obtained enabled them to be cut using a diamond wire saw into samples of appropriate shape and size for the determination of their geometric density. For an equal amount of material and regardless of the sintering parameters, the thickness of the NBG monoliths is double that of the BG samples, which suggests a greater porosity. Note that contrary to BG monoliths, NBG monoliths were obtained even in the absence of added solvent. This suggests that NBG powders may contain some residual water. The monoliths with the best specific surface areas were selected for the bioactivity tests.

### 1.3. Preparation of SBF

The simulated body fluid (SBF) solution has an ionic composition similar to that of human blood plasma. The SBF solution was prepared according to Kokubo's protocol [21] and previous work [17]. The preparation of 1 L of SBF was realized by mixing Ca-SBF and P-SBF solutions (500 cm<sup>3</sup> each). 1 L of Ca-SBF and P-SBF solutions each was prepared at 37°C by dissolving in distilled water, respectively: 0.7349g CaCl<sub>2</sub>·2H<sub>2</sub>O, 0.6095g MgCl<sub>2</sub>·6H<sub>2</sub>O and 0.3484g K<sub>2</sub>HPO<sub>4</sub>, 0.7056g NaHCO<sub>3</sub>, 0.4473g KCl, 16.1061g NaCl. After complete dissolution of the salts, the pH was adjusted to 7.4 with 6.057g Tris C<sub>4</sub>H<sub>11</sub>NO<sub>3</sub> (Tris-hydroxymethyl aminomethane or Tris) and HCl 6 N.

## 2. Characterization

1 X-Ray Diffraction (XRD) patterns were collected at room temperature in the  $2\theta$  range 20-80° with a  
2 step size of 0.026° and a scan time per step of 40 s using a PANalytical X'Pert Pro diffractometer (Cu-  
3 L2,L3 radiation,  $\lambda = 1.5418 \text{ \AA}$ , 40 kV, 40 mA, PIXcel 1D detector). Data Collector and High-Score Plus  
4 softwares were used, respectively, for recording and analysis of the patterns. XRD analysis, after  
5 immersion in SBF, was performed on sample surfaces. Thermal analyses were performed on a Labsys  
6 evo 1600TG-DTA/DSC (Setaram) with a heating rate of  $10 \text{ K}\cdot\text{min}^{-1}$  in nitrogen. The Fourier Transform  
7 Infrared (FTIR) transmittance spectra of the powdered glass samples were recorded using a FTIR  
8 spectrometer (Alpha Bruker Banner Lane, Coventry), in the  $400\text{--}2000 \text{ cm}^{-1}$  range, at room  
9 temperature, after mixing 1 mg of the glass with 100 mg of dried KBr. For FTIR analysis after immersion  
10 in SBF, powdered samples were scratched from pellet surfaces and diluted in KBr as previously  
11 described.

12 Nitrogen adsorption isotherms were measured at 77 K on a 3Flex adsorption analyzer from  
13 Micromeritics (Norcross, GA, USA). Prior to measurements, the samples were outgassed overnight at  
14 ambient temperature in a VacPrep degas system. Specific surface areas ( $S_{\text{BET}}$ ) were derived from the  
15 isotherms using the BET equation and a set of 6 experimental points of the linear range of the BET plot  
16 ( $0.05 < P/P^0 < 0.3$ ). In addition, the method provides the total pore volume of the samples. X-ray  
17 tomography has been investigated as complementary technique to  $\text{N}_2$  physisorption measurements to  
18 visualize porosity higher than  $20 \text{ \mu m}$  [24] using a A V|tome|X apparatus (GE) equipped with a  
19 2024x2024 pixels flat panel XRD detector and a GE 180 kV transmission tube. The scans were acquired  
20 at an accelerating voltage of 80 kV, a current of  $200 \text{ \mu mA}$  with no beam hardening filters. 1500  
21 projections were taken, each being the average of 2 radiographs with an exposure time of 1s. The voxel  
22 size was  $7 \text{ \mu m}$  and the scan total duration was about 1 hour.

23 Particle size analysis of bioglass powders after grinding and before sintering was performed using a  
24 Laser Particle Sizer Analysette 22 NanoTec (FRITSCH GmbH). Powders were dispersed in water and  
25 exposed to ultrasounds during analysis. Powders density was determined by dividing the sample  
26 weight by the volume measured by gas (He) displacement pycnometry using AccuPyc 1330  
27 pycnometer from Micromeritics. Volume was averaged from 5 measurements.

28 Prior to *in vitro* bioactivity tests, the bioglass monoliths (of 10 mm diameter and few millimeters  
29 thick) were embedded in a resin so as to expose only one face of the pelleted samples to the SBF  
30 solution to ensure for each sample identical exposition to SBF and further comparison possible. The  
31 samples were subsequently placed in an incubator at  $37^\circ\text{C}$  under a controlled agitation of  $50 \text{ revs min}^{-1}$   
32 for fixed immersion times (1, 3, 7, 15 and 30 days). To analyse the ionic exchanges that took place  
33 between the surface of the immersed biomaterial and the synthetic physiological liquid, Inductively  
34 Coupled Plasma Atomic Emission Optical Spectroscopy (ICP-OES, iCAP 7000Series, Thermo Scientific)  
35 analysis was performed under argon flux to measure concentrations of silicon (Si), phosphorus (P) and  
36 calcium (Ca) on 10 mL sampling of SBF solution after each immersion time.

1 Surface morphology of the samples was examined before and after immersion in SBF by Scanning  
2 Electron Microscopy (SEM) with a JEOL JSM IT300 equipment (CMEBA, university of Rennes 1). Prior  
3 to SEM observations, the samples were metallized with gold.

### 4 **3. Results and discussion**

#### 5 **3.1. Bioglass powders characterization**

6 Fig. 2 presents the XRD patterns of the NBG and BG bioglass powders. The patterns show only  
7 diffusion halos that confirms the amorphous glass structure of both synthesized powders. This result  
8 corroborates with DTA analysis, presented in supplementary data (Fig. S1), which allows to determine  
9 the characteristic glass transition, crystallization and melting temperatures.

10 The FTIR spectra, in the 400–2200  $\text{cm}^{-1}$  spectral range, of NBG and BG bioglass powders are quite  
11 similar (Fig. 3). Bands characteristic of the vibrations associated to the silicate network observed at  
12 466/502, 788/740, 940/923 and 1060/1032  $\text{cm}^{-1}$  are assigned respectively to Si-O-Si bending mode, Si-  
13 O-Si symmetric stretching mode of bridging oxygen atoms between tetrahedra, Si-O-Si stretching  
14 mode of non-bridging oxygen atoms and Si-O-Si asymmetric stretching mode of bridging oxygen atoms  
15 within the tetrahedra [13, 25–27]. The band located at 563/592 $\text{cm}^{-1}$  is attributed to P-O bending  
16 vibrational mode of  $\text{PO}_4^{3-}$  group in amorphous phosphate [25,26] and the band at 1170  $\text{cm}^{-1}$  is  
17 attributed to P=O stretching mode [25].The band at about 1630  $\text{cm}^{-1}$  can be assigned to molecular  
18 water contained in bioglass powders or adsorbed on powder surfaces [25,26,28]. Finally small bands  
19 observed at about 1400  $\text{cm}^{-1}$  are assigned to atmospheric  $\text{CO}_2$ . The slight differences (band shifts)  
20 between the two spectra are due to the presence of  $\text{Na}_2\text{O}$  in BG which, as network modifier, brings  
21 about modifications to the glassy network (creation of non-bridging oxygen) [13].

22 The particle size distribution of the bioglass powders determined by laser scattering is represented  
23 in terms of a histogram and a cumulative size distribution in Fig.4. The NBG powder displays a major  
24 monomodal distribution of nanometric size (<100 nm) with some agglomerates between 2 and 30  
25 microns while the coarse and fine BG powders present major monomodal distributions centered  
26 respectively on 60  $\mu\text{m}$  and 30  $\mu\text{m}$ .

#### 27 **3.2. Bioglass monoliths characterization**

##### 28 **3.2.1. Physisorption-Structure**

29 Nitrogen adsorption-desorption isotherms were measured at 77 K on the monoliths samples  
30 elaborated by HyHP according to the sintering parameters reported in Table 1. All NBG monoliths have  
31 adsorption-desorption isotherms similar to that presented in Fig.5a. With a hysteresis loop (H1 type)  
32 associated with capillary condensation taking place in mesopores and some limiting uptake at high  
33 relative pressures, the isotherms are of type IV, characteristic of mesoporous materials, as classified in  
34 [29]. Coarse and fine BG samples have similar isotherms, classified as type II, characteristic of non-  
35 porous or macroporous solid (Fig.5b) [25,29].

The density of NBG powders measured by gas displacement pycnometry was  $2.48 \pm 0.02 \text{ g/cm}^3$ . This value which is less than that expected from the composition ( $2.91 \pm 0.01 \text{ g/cm}^3$ ) is attributed, as considered previously (paragraphs 1.2 and 3.1), to the residual water contained in the NBG powders (Supplementary data, Fig. S1). The density measured for BG powders was  $2.71 \pm 0.02 \text{ g/cm}^3$ , in agreement with the glass composition close to that of Bioglass® 45S5 [30]. Table 2 reports the geometric density of the monoliths after hydrothermal sintering and their resulting porosity, the specific surface areas determined by BET method and total pore volumes.

Table 2  
Geometric density, porosity,  $S_{\text{BET}}$ , total pore volume of NBG and BG monoliths (0.2g powder, 0.5kN).

Sample	Time (min)	Solvent	Vol ( $\mu\text{L}$ )	T ( $^{\circ}\text{C}$ )	Density ( $\text{g/cm}^3$ )	Porosity (%)	$S_{\text{BET}}$ ( $\text{m}^2/\text{g}$ )	Pore volume ( $\text{cm}^3/\text{g}$ )
<b>NBG</b>								
<b>NBG powder</b>							175	0.757
NBG-231	30	NaOH-2M	80	150	0.74	71	101	0.404
NBG-232	30	H <sub>2</sub> O	80	150	0.67	73	146	0.641
NBG-255	5	no	no	150	0.69	72	164	0.680
NBG-256	5	NaOH-2M	80	150	0.71	72	99	0.381
NBG-257	5	H <sub>2</sub> O	80	150	0.67	73	148	0.621
NBG-259	5	NaOH-2M	160	150	0.73	71	77	0.256
NBG-260	5	NaOH-2M	240	150	0.76	70	72	0.268
<b>Coarse BG powder</b>							0.4	0.0004
BG-264	5	NaOH-2M	60	150	1.48	45	8	0.006
<b>Fine BG powder</b>							0.5	0.0005
BG-229	5	NaOH-2M	80	150	1.53	43	6	0.004

The porosity measurements confirm the hypothesis of a greater porosity in NBG monoliths that we previously deduced from their thicknesses. The large specific surface area of NBG samples, up to 15-20 times that of BG samples, can be explained by their mesoporosity and large pore volumes. The porosity content of NBG monoliths is nearly the same ( $\approx 70\%$ ) in comparison to the various hydrothermal sintering parameters by the fact that the approximation on porosity could reach  $\pm 3\%$ . However, significant differences are observed in terms of specific surface area ( $S_{\text{BET}}$ ) depending on the amount and nature of solvent. The decrease in the amount of NaOH-2M from 240 to 80 mL (NBG-260/259/256) is accompanied by a non significant increase in porosity (from 70% to 72%) but strongly limits the  $S_{\text{BET}}$  decrease compared to the initial powder (59% decrease for 240 mL versus 43% decrease for 80 mL). Our hypothesis is that NaOH as basic solvent removes, in the first few minutes, the surface roughness of the powder particles with which it comes in contact, reducing the specific surface area. This effect is enhanced by increased NaOH volume. Moreover, if we compare the sintering in the presence of H<sub>2</sub>O or NaOH-2M (see NBG-231 vs NBG-232 and NBG-256 vs NBG-257),  $S_{\text{BET}}$  is lowered by approximately 30% in the presence of NaOH for both sintering times. The surface areas are maintained at about  $150 \text{ m}^2/\text{g}$  in the presence of H<sub>2</sub>O while they drop to about  $100 \text{ m}^2/\text{g}$  in the presence of NaOH due to its caustic effect, as previously mentioned. The increase in HyHP dwell time has though no effect

1 on the specific surface area and the porosity. For BG samples, the larger surface areas of monoliths  
2 compared to powders can be explained by the reduction in grain size induced by the dissolution-  
3 precipitation mechanism whose effect is more pronounced for coarser powders. It should be noted  
4 that this hydrothermal sintering process offers compared to conventional sintering (solid state  
5 diffusion) the major advantage of producing monoliths with finer grains than those of the precursor  
6 powders.  
7

8 In previous work, Ndayishimiye *et al* reported on the HyHP sintering conditions (same equipment)  
9 of LSMO ( $\text{La}_{0.66}\text{Sr}_{0.34}\text{MnO}_3$ )- $\text{SiO}_2$  composites and silica in presence of NaOH and water solvents,  
10 respectively [31,32]. Sintering conditions were slightly different to our conditions (high external force  
11 applied for hours in presence of a mineralizer) as the objective was to maximize the densification. It  
12 was observed that NaOH solvent induces a better sintering than  $\text{H}_2\text{O}$  due to a higher intergranular  
13 dissolution (mineralizer effect) and precipitation inside the free space porosity between the particles  
14 which results in a decrease in porosity content [33]. In the present work, more gentle conditions were  
15 used so as to control the dissolution-precipitation phenomena in order to consolidate (and not densify)  
16 the powders and create a large quantity of porosities. Indeed, monoliths with good mechanical  
17 strength (allowing their handling) were produced at low temperature ( $150^\circ\text{C}$ ) under a low external  
18 force (0.5 kN) applied for only 5 min. These conditions achieve sufficient consolidation by formation of  
19 necks (first sintering stage). The sintering process seems to be stopped after 5 min as surface areas  
20 and porosity values are unchanged after 30 min-HyHP explaining the large porosity values.  
21

22 Finally, the tests carried out in absence of solvent (NBG 255) give the best results in terms of  
23 porosity (73%) and specific surface area (only 6% reduction compared to the initial powder). As  
24 mentioned previously, the initial powder contained chemisorbed water which is released by heating.  
25 The quantity of water measured by TGA at  $150^\circ\text{C}$  (sintering temperature) in the initial 0.2g NBG powder  
26 ( $\sim 3\%$  in weight) is about  $6\mu\text{L}$  (Fig. S1). This quantity, though small, proves to be sufficient to produce  
27 the hydrothermal conditions necessary for sintering; the addition of water is therefore not essential  
28 for sintering naturally hydrated NBG nanopowders.  
29

30 We have also determined the rate of open porosities from density measured by the impregnation  
31 method in water based on Archimedes principle [34]. Results are presented in supplementary data  
32 (Table S1). We found that the percentage of open porosity is close to the rate of porosity determined  
33 geometrically reported in Table 2. The monoliths thus obtained have essentially open porosity proving  
34 the HyHP effectiveness of processing interconnected porous structures.  
35

36 Tomography has been used as complementary experimental method to visualize pores larger than  
37  $20\mu\text{m}$  (voxel:  $7\mu\text{m}$ ). Fig. 6 shows large pores of about  $60\mu\text{m}$  size in coarse BG samples (Fig. 6(a)) and  
38 smaller pores ( $20\mu\text{m}$  or less) in fine BG samples confirming BG-based samples are macroporous in  
39 accordance with the physisorption characterization (Fig. 5). In contrast, tomography images of NBG  
40 samples do not present any visible macroporosity at this scale level. Let us recall that physisorption  
41 characterization revealed the presence of mesopores (2-50 nm) in NBG samples.-NBG monoliths are  
42  
43  
44  
45  
46  
47  
48  
49  
50  
51  
52  
53  
54  
55  
56  
57  
58  
59  
60  
61  
62  
63  
64  
65

1  
2  
3  
4  
5  
6  
7  
8  
9  
10  
11  
12  
13  
14  
15  
16  
17  
18  
19  
20  
21  
22  
23  
24  
25  
26  
27  
28  
29  
30  
31  
32  
33  
34  
35  
36  
37  
38  
39  
40  
41  
42  
43  
44  
45  
46  
47  
48  
49  
50  
51  
52  
53  
54  
55  
56  
57  
58  
59  
60  
61  
62  
63  
64  
65

obtained with 70% of porosity which remains mainly open. No results exist in the literature which achieve such a high percentage of porosity in bioglass monoliths. To date, a maximum porosity of 60% is reported for bioactive glass scaffolds processed by additive manufacturing techniques [1]. While it is generally admitted that it is difficult to obtain high levels of porosity (>50%) with interconnected porosity, we demonstrated that our technique can efficiently process bioglass powders into porous structures while retaining the amorphous glass structure. In the next step, HyHP technique was applied to process a structure with gradients of porosity by co-sintering coarse and fine BG powders. Fig.5(d) shows such a monolith with distinguishable coarse BG on top and fine BG at the bottom. This demonstration proves the ability of the technique to process scaffolds with different scales of porosity to mimic the structure of porous bone. The literature reported so far only mention the combination of different techniques (sol-gel, co-polymer templates or sacrificial methyl cellulose templates, rapid prototyping technique) to achieve combined (giant)-macro-mesoporosity [35,36].

Following these observations, the *in vitro* bioactivity tests were performed on NBG 255 and NBG 257 samples showing the best specific surface/porosity (likely to induce better bioactivity) and compared to those of BG samples.

### 3.2.2. *In vitro* bioactivity tests

*In vitro* tests were performed according to a method in which a SBF solution is used in the *in vitro* evaluation of the formation of a HA layer on the surface of the bioglass scaffolds.

#### 3.2.2.1. XRD characterization

##### a) NBG monoliths

Fig. 7 presents the XRD patterns of the surface of samples NBG 255 and 257 at fixed immersion times (0, 1, 3, 7, 15 and 30 days). The XRD pattern of synthetic HA ( $\text{Ca}_{10}(\text{PO}_4)_6(\text{OH})_2$ , calcium hydroxyde phosphate AR powder, Alfa) is included as reference. NBG 255 and NBG 257 samples show the characteristic lines of the HA from the first day of immersion in the SBF with the major lines (002) and (211) appearing distinctly at about  $26^\circ(2\theta)$  and  $32^\circ(2\theta)$  respectively. The lines intensities increase with the immersion time proving the growth of the HA layer and after 7 days of immersion, it is possible to distinguish some secondary lines such as the (130), (222) and (213) reflections of HA phase. These results indicate that bioactivity reactions reached within 1 day the final stage (stage 5) of the proposed stages for *in vitro* HA formation in SBF [1,37].

##### b) BG monoliths

Fig. 8 presents the XRD patterns of the surface of BG 264 and BG 229 samples at fixed immersion times (0, 1, 3, 7, 15 and 30 days) as well as that of HA as reference. The patterns do not show any diffraction lines except very small lines of calcite ( $\text{CaCO}_3$ ) at  $29.4^\circ(2\theta)$  (card JCPDS n° 85-1108). The patterns appear the same after 15 days of immersion. This suggests that stage 4 of bioactivity process

has barely begun in this period. This result is consistent with bioactivity tests that were reported on BG powders which showed HA characteristic lines only after 15 days of immersion [16].

#### 3.2.2.2. FTIR analysis

After immersion in the SBF, the characteristic bands in Fig. 3 are modified due to chemical reactions on the surface of the bioactive glass leading to the formation of HA. Fig. 9 shows the FTIR spectra of NBG 257 and BG 264 samples before and after exposure to SBF solution for 0-15 days. The FTIR spectrum of HA is included as reference. It is worth mentioning that FTIR spectra of NBG 255 and BG 229 samples are so similar, respectively, to those of NBG 257 and BG 264 that only NBG 257 and BG 264 spectra are reported for clarity. We observe for NBG 257, from the first immersion day, the presence of P-O bands at 565, 603 and 1039  $\text{cm}^{-1}$  which are characteristic of crystalline phosphates and confirm the formation of calcium phosphate layer on the monolith surface. C-O bands at 874 and 1420  $\text{cm}^{-1}$  are also revealed. The presence of characteristic bands of carbonate groups proves the formation of a layer of carbonated hydroxyapatite (HCA) on the surface of the monoliths in contact with SBF. For BG 264 sample, we observe that the characteristic bands are deformed and/or shifted from the first day of immersion. These deformations indicate the formation of a silica-rich layer on the glass surface during stage 3 of the bioactivity process. Yet, the formation of HA proceeds only after 15 days of immersion.

#### 3.2.2.3. SEM characterization

SEM analyses provided detailed observations of the surface of the monoliths as a function of the immersion time in the SBF. Fig. 10 shows surface micrographs of NBG 257 and BG 264 samples before and after soaking in SBF for 1 to 7 days. Significant changes in surface morphology can be observed for NBG samples from 1 day of immersion whereas BG surface is not modified even after 7 days of immersion (the glass surface is still visible). As can be observed, only after 1 day of immersion, NBG surfaces, initially made of partially sintered spherical particles, present the typical morphology of HA (elongated particles) [12,13]. On the contrary, images of BG surfaces exhibit similar morphologies for 7 days duration of bioactivity tests. All these observations are in agreement with the XRD patterns and IR spectra obtained for the same immersion times. These observations attest that NBG samples are more bioactive than BG samples.

#### 3.2.2.4. ICP-OES characterization

The concentrations of silicon, calcium and phosphorus species present in SBF solution were measured by ICP-OES as a function of soaking time to monitor the kinetics of consumption and release of these elements occurring during the bioactivity process (Fig. 11). Fig. 11(a) shows a significant release of Si from the first immersion day and a similar profile over the immersion time for all samples. This release is the consequence of stage 2 of the bioactivity process characterized by the loss of soluble silica  $\text{Si}(\text{OH})_4$  by rupture of the Si-O-Si bonds. Fig. 11(b) shows that the P concentration decreases rapidly over the first day of dissolution and, considering P composition ( $\text{P}_2\text{O}_5$  in mol%: 5.0% for NBG vs

2.6% for BG), that the consumption is much faster for NBG than BG. Concurrent with the Si concentration increase, this decrease in P concentration is attributed to the incorporation of P ions from the dissolution medium within the Ca-P rich reaction layer forming on the glass surface. NBG is so reactive that all available P is consumed within 3 days of immersion. The P release occurs less rapidly and over a longer period of time (> 15 days) in BG monoliths. Fig. 11(c) shows differences between NBG and BG in Ca dissolution profiles. For NBG, Ca concentration increases until day 3 then decreases continuously to its initial value after 30 days. The Ca release corresponds to stage 1 of the bioactivity mechanism in which  $\text{Ca}^{2+}$  ions exchange rapidly with  $\text{H}^+$  from solution (dealkalinization) creating silanol bonds ( $\text{Si-OH}$ ) on the glass surface. The consumption corresponds to stage 4 in which  $\text{Ca}^{2+}$  ions migrate from the SBF to the surface of the bioactive glass to form a film rich in amorphous  $\text{CaO-P}_2\text{O}_5$ . The Ca concentration observed for BG samples, on the other hand, decreased continuously (stage 4). The compositional and morphological differences between NBG and BG may account for the observed dissolution profiles. The higher CaO content (40.0% in mol% for NBG vs 26.4% for BG) and high surface areas of NBG samples explain the calcium release whereas for BG samples the lower CaO content, the less porous surfaces and lower surface areas limit the dissolution rate and Ca release. These results are in agreement with those reported by Sepulveda *et al* [38] on the dissolution behavior of melt-derived and sol-gel derived bioactive glasses. This study showed indeed that the higher CaO content in sol-gel composition accounts for the higher calcium concentration released in SBF and faster saturation of calcium and phosphate ions, conditions that accelerate the kinetics of an apatite layer precipitation. This mechanism is supported, as in [38], by the faster depletion of phosphorous in SBF that we observed for sol-gel derived monoliths. The superior bioactivity of NBG monoliths, confirmed by FTIR-XRD analyses and SEM observations that proved the formation of a HCA layer on the bioglass, is attributed to the highly porous bioglass surfaces that our HyHP technique was able to produce from sol-gel nanometric powders.

#### 4. Conclusions

In this study, the processing of porous bioglass monoliths using HyHP technique is reported for the first time. This process makes it possible to obtain, in a single step, structures with open porosities of different size depending on the characteristics of the precursor powders themselves depending on the synthesis method. We have thus shown that HyHP applied on sol-gel derived glass powders build monoliths with >70% open porosity whereas applied on melt-derived glass powders, the open porosity is at most 45%. The high porosity content in NBG monoliths results from their mesoporosity induced by the nanometric size of the precursor powders. Contrary to BG powders, the sintering of NBG powders occurs in absence of a mineralizer (NaOH) and can proceed, additionally, in absence of  $\text{H}_2\text{O}$  that they already contain. All the monoliths sintered at only 150°C for 5 min present notable mechanical strength and can be cut by a diamond wire saw. Finally, we have shown that our technique can process 3D structures with gradient of porosity. Our HyHP technique proves to be a real

breakthrough in the realization of consolidated bioglasses with controlled porosity to be adapted to various implantation sites. In addition, as single-step, low temperature and short time process (150°C, 5 min), this technique is a cost-effective and eco-efficient alternative for sintering biomaterials to conventional and 3D techniques.

## Acknowledgments

We thank Ms Lisa Andrey for her contribution to the HyHP experiments at ICMCB UMR5026, as part of her Master 2 internship.

## References

- [1] J.R. Jones, Review of bioactive glass: From Hench to hybrids, *Acta Biomater.* 9 (2013) 4457–4486. <https://doi.org/10.1016/j.actbio.2012.08.023>.
- [2] F. Baino, E. Fiume, J. Barberi, S. Kargozar, J. Marchi, J. Massera, E. Verné, Processing methods for making porous bioactive glass-based scaffolds—A state-of-the-art review, *Int. J. Appl. Ceram. Technol.* 16 (2019) 1762–1796. <https://doi.org/10.1111/ijac.13195>.
- [3] G. Demazeau, A. Largeteau, Hydrothermal/solvothermal crystal growth: an old but adaptable process: Hydrothermal/solvothermal crystal growth, *Z. Anorg. Allg. Chem.* 641 (2015) 159–163. <https://doi.org/10.1002/zaac.201400515>.
- [4] G. Gautam, Processing of biomaterials for bone tissue engineering: State of the art, *Materials Today: Proceedings*. <https://doi.org/10.1016/j.matpr.2021.09.459>.
- [5] X. Ren, Q. Tuo, K. Tian, G. Huang, J. Li, T. Xu, X. Lv, J. Wu, Z. Chen, J. Weng, Q. Wang, Y. Mu, Enhancement of osteogenesis using a novel porous hydroxyapatite scaffold in vivo and vitro, *Ceram. Int.* 44 (2018) 21656–21665. <https://doi.org/10.1016/j.ceramint.2018.08.249>.
- [6] Z. Chen, X. Zhang, Y. Yang, K. Zhou, N. Wragg, Y. Liu, M. Lewis, C. Liu, Fabrication and characterization of 3D complex hydroxyapatite scaffolds with hierarchical porosity of different features for optimal bioactive performance, *Ceram. Int.* 43 (2017) 336–344. <https://doi.org/10.1016/j.ceramint.2016.09.160>.
- [7] N. Yamasaki, T. Kai, M. Nishioka, K. Yanagisawa, K. Ioku, Porous hydroxyapatite ceramics prepared by hydrothermal hot-pressing, *J Mater Sci Lett.* 9 (1990) 1150–1151. <https://doi.org/10.1007/BF00721872>.
- [8] A. Nakahira, T. Murakami, T. Onoki, T. Hashida, K. Hosoi, Fabrication of porous hydroxyapatite using hydrothermal hot pressing and post-sintering *J. Am. Ceram. Soc.*, 88 [5] (2005) 1334–1336. DOI: 10.1111/j.1551-2916.2005.00238.x
- [9] Z. Matamoros-Veloza, J.C. Rendón-Angeles, K. Yanagisawa, E.E. Mejia-Martínez, J.R. Parga, Low temperature preparation of porous materials from TV panel glass compacted via hydrothermal hot pressing, *Ceram. Int.* 41 (2015) 12700–12709. <https://doi.org/10.1016/j.ceramint.2015.06.102>.
- [10] Z. Matamoros-Veloza, J.C. Rendón-Angeles, K. Yanagisawa, M.A. Cisneros-Guerrero, M.M. Cisneros-Guerrero, L. Aguirre, Preparation of foamed glasses from CRT TV glass by means of hydrothermal hot-pressing technique, *J. Eur. Ceram. Soc.* 28 (2008) 739–745. <https://doi.org/10.1016/j.jeurceramsoc.2007.09.014>.
- [11] R.L. Siqueira, O. Peitl, E.D. Zanotto, Gel-derived SiO<sub>2</sub>–CaO–Na<sub>2</sub>O–P<sub>2</sub>O<sub>5</sub> bioactive powders: Synthesis and in vitro bioactivity, *Mater. Sci. Eng. C.* 31 (2011) 983–991. <https://doi.org/10.1016/j.msec.2011.02.018>.
- [12] J. Chevalier, L. Gremillard, Ceramics for medical applications: A picture for the next 20 years, *J. Eur. Ceram. Soc.* 29 (2009) 1245–1255, doi:10.1016/j.jeurceramsoc.2008.08.025
- [13] M. Vallet-Regí, C.V. Ragel, A.J. Salinas, Glasses with medical applications, *Eur. J. Inorg. Chem.* (2003) 1029–1042. <https://doi.org/10.1002/ejic.200390134>.
- [14] Q.L. Loh, C. Choong, Three-dimensional scaffolds for tissue engineering applications: Role of porosity and pore size, *Tissue Eng. Part B Rev.* 19 (2013) 485–502. <https://doi.org/10.1089/ten.teb.2012.0437>.

- [15] E. Dietrich, Synthèse et études physico-chimiques de verres bioactifs denses et poreux. Applications en tant que biomatériaux en sites osseux, PhD Dissertation, Université de Rennes 1 (2008)
- [16] X.V. Bui, Elaboration de biomatériaux verres-substances actives (zolédrone-chitosane). Caractérisations physico-chimiques. Expérimentations "in vitro", PhD Dissertation, Université de Rennes 1 (2011)
- [17] N. Rocton, Élaboration de bioverres et de nanobioverres ostéoinducteurs associés à des molécules à usage thérapeutique. PhD Dissertation, Université de Rennes 1 (2019)
- [18] X.V. Bui, H. Oudadesse, Y. Le Gal, O. Merdrignac-Conanec, G. Cathelineau, Bioactivity behaviour of biodegradable material comprising bioactive glass, *Korean J. Chem. Eng.* 29 (2012) 215–220. <https://doi.org/10.1007/s11814-011-0151-0>.
- [19] E. Wers, H. Oudadesse, B. Lefeuvre, B. Bureau, O. Merdrignac-Conanec, Thermal investigations of Ti and Ag-doped bioactive glasses, *Thermochim. Acta.* 580 (2014) 79–84. <https://doi.org/10.1016/j.tca.2014.02.001>.
- [20] E. Wers, H. Oudadesse, B. Lefeuvre, O. Merdrignac-Conanec, A. Barroug, Evaluation of the kinetic and relaxation time of gentamicin sulfate released from hybrid biomaterial Bioglass-chitosan scaffolds, *Appl. Surf. Sci.* 353 (2015) 200–208. <https://doi.org/10.1016/j.apsusc.2015.06.146>.
- [21] T. Kokubo, H. Takadama, How useful is SBF in predicting in vivo bone bioactivity?, *Biomaterials.* 27 (2006) 2907–2915. <https://doi.org/10.1016/j.biomaterials.2006.01.017>.
- [22] A. Ndayishimiye, A. Largeteau, M. Prakasam, S. Pechev, M.-A. Dourges, G. Goglio, Low temperature hydrothermal sintering process for the quasi-complete densification of nanometric  $\alpha$ -quartz, *Scr. Mater.* 145 (2018) 118–121. <https://doi.org/10.1016/j.scriptamat.2017.10.023>.
- [23] A. Largeteau, M. Prakasam, Trends in high pressure developments for new perspectives, *Solid State Sci.* 80 (2018) 141–146. <https://doi.org/10.1016/j.solidstatesciences.2018.04.012>.
- [24] J. Baruchel, J.-Y. Buffière, E. Maire, P. Merle, G. Peix, in: *X-Ray Tomography in Material Science*, HERMES Science Publications, Paris, 2000.
- [25] H.A. ElBatal, M.A. Azooz, E.M.A. Khalil, A. Soltan Monem, Y.M. Hamdy, Characterization of some bioglass-ceramics, *Mater. Chem. Phys.* 80 (2003) 599–609. [https://doi.org/10.1016/S0254-0584\(03\)00082-8](https://doi.org/10.1016/S0254-0584(03)00082-8).
- [26] L.A. Adams, E.R. Essien, R.O. Shaibu, A. Oki, Sol-gel synthesis of  $\text{SiO}_2$ -CaO- $\text{Na}_2\text{O}$ - $\text{P}_2\text{O}_5$  bioactive glass ceramic from sodium metasilicate. *New J. Glass Ceram.* 03 (2013) 11–15. <https://doi.org/10.4236/njgc.2013.31003>.
- [27] T.T. Swe, H. Mohamad, K.A. Shariff, A.A. Thant, Fabrication of sol-gel derived new quaternary silicate Bioglass S55P4, in: *Kelantan, Malaysia, 2019*: p. 020070. <https://doi.org/10.1063/1.5089369>.
- [28] J. Weng, Formation and characteristics of the apatite layer on plasma-sprayed hydroxyapatite coatings in simulated body fluid, *Biomaterials.* 18 (1997) 1027–1035. [https://doi.org/10.1016/S0142-9612\(97\)00022-7](https://doi.org/10.1016/S0142-9612(97)00022-7).
- [29] J. Lykiema, K.S.W. Sing, J. Haber, M. Kerker, E. Wolfram, J.H. Block, N.V. Churaev, D.H. Everett, R.S. Hansen, R.A.W. Haul, J.W. Hightower, R.J. Hunter, Prepared for publication by the Subcommittee on Reporting Gas Adsorption Data Consisting of K. S. W. SING (UK, Chairman); D. H. EVERETT (UK); R. A. W. HAUL (FRG); L. MOSCOU (Netherlands); R. A. PIEROTTI (USA); J. ROUQUEROL (France); T. SIEMIENIEWSKA (Poland), (1984) 17.
- [30] L.L. Hench, J. Wilson, *An Introduction to Bioceramics*, World Scientific, Singapore, 1993.
- [31] A. Ndayishimiye, S. Buffière, M.-A. Dourges, A. Largeteau, M. Prakasam, S. Mornet, O. Kaman, J. Zdeněk, J. Hejtmánek, G. Goglio, Design of 0–3 type nanocomposites using hydrothermal sintering, *Scr. Mater.* 148 (2018) 15–19. <https://doi.org/10.1016/j.scriptamat.2018.01.013>.
- [32] A. Ndayishimiye, A. Largeteau, S. Mornet, M. Duttine, M.-A. Dourges, D. Denux, M. Verdier, M. Gouné, T. Hérisson de Beauvoir, C. Elissalde, G. Goglio, Hydrothermal sintering for densification of silica. Evidence for the role of water, *J. Eur. Ceram. Soc.* 38 (2018) 1860–1870. <https://doi.org/10.1016/j.jeurceramsoc.2017.10.011>.
- [33] G. Goglio, A. Ndayishimiye, A. Largeteau, C. Elissalde, View point on hydrothermal sintering: Main features, today's recent advances and tomorrow's promises, *Scr. Mater.* 158 (2019) 146–152. <https://doi.org/10.1016/j.scriptamat.2018.08.038>.
- [34] Y.-B.P. Kwan, J.R. Alcock, The impact of water impregnation method on the accuracy of open porosity measurements, *J. Mater. Sci.* 37 (2002) 2557 – 2561

[35] H. Yun, S. Kim, Y. Hyeon, Design and preparation of bioactive glasses with hierarchical pore networks, *Chem. Commun.* (2007) 2139–2141. <https://doi.org/10.1039/b702103h>.

[36] A. García, I. Izquierdo-Barba, M. Colilla, C.L. de Laorden, M. Vallet-Regí, Preparation of 3-D scaffolds in the  $\text{SiO}_2\text{-P}_2\text{O}_5$  system with tailored hierarchical meso-macroporosity, *Acta Biomater.* 7 (2011) 1265–1273. <https://doi.org/10.1016/j.actbio.2010.10.006>.

[37] L. L. Hench, Bioceramics: from concept to clinic, *J. Am. Ceram. Soc.* 74 [7] (1991) 1487-510

[38] P. Sepulveda, J.R. Jones, L.L. Hench, In vitro dissolution of melt-derived 45S5 and sol-gel derived 58S bioactive glasses, *J. Biomed. Mater. Res.* 61 (2002) 301–311. <https://doi.org/10.1002/jbm.10207>.

1  
2  
3  
4  
5  
6  
7  
8  
9  
10  
11  
12  
13  
14  
15  
16  
17  
18  
19  
20  
21  
22  
23  
24  
25  
26  
27  
28  
29  
30  
31  
32  
33  
34  
35  
36  
37  
38  
39  
40  
41  
42  
43  
44  
45  
46  
47  
48  
49  
50  
51  
52  
53  
54  
55  
56  
57  
58  
59  
60  
61  
62  
63  
64  
65

## Figures captions

Fig.1. External view of HyHP equipment and internal schematic view of the autoclave

Fig.2. XRD patterns of BG and NBG bioglass powders

Fig.3. FTIR spectra of BG and NBG bioglass powders

Fig.4: Particle size distribution of NBG and BG bioglass powders (ultrasonicated and water-dispersed during analysis)

Fig.5. Typical N<sub>2</sub> adsorption-desorption isotherms measured at 77K on (a) NBG monoliths and (b) BG monolith with photographs in inset

Fig. 6. Tomography images of (a) coarse BG, (b) fine BG and (c) NBG monoliths (d) BG gradient monolith processed by HyHP at 150°C - 5min - 0,5kN (diam: 10 mm)

Fig. 7. XRD patterns of surfaces of (a) NBG 255 and (b) NBG 257 monoliths at different immersion times in SBF

Fig. 8. XRD patterns of surfaces of (a) BG 264 and (b) BG 229 monoliths at different immersion times in SBF

Fig. 9. FTIR spectra of NBG 257 and BG 264 samples before and after soaking in SBF solution at different immersion times

Fig. 10. SEM micrographs of surfaces of NBG and BG monoliths processed by HyHP

Fig. 11: (a) Si (b) P (c) Ca elemental concentration in SBF as a function of immersion time

1  
2  
3  
4  
5  
6  
7  
8  
9  
10  
11  
12  
13  
14  
15  
16  
17  
18  
19  
20  
21  
22  
23  
24  
25  
26  
27  
28  
29  
30  
31  
32  
33  
34  
35  
36  
37  
38  
39  
40  
41  
42  
43  
44  
45  
46  
47  
48  
49  
50  
51  
52  
53  
54  
55  
56  
57  
58  
59  
60  
61  
62  
63  
64  
65

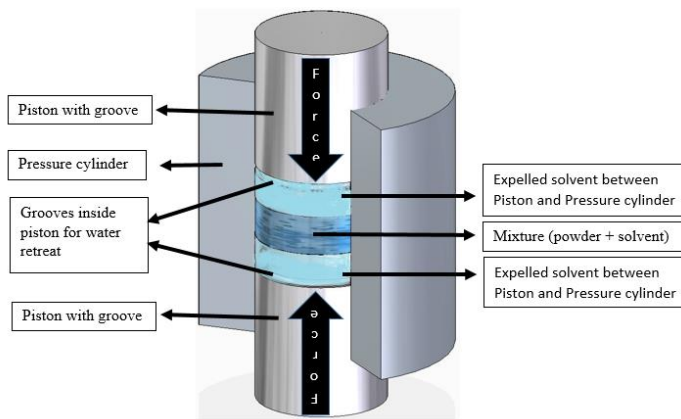
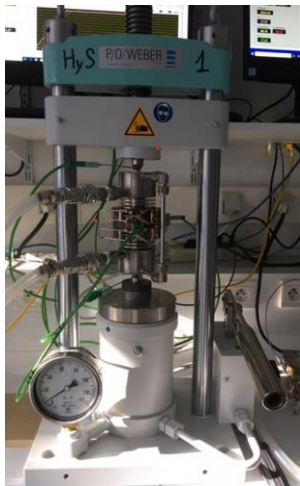


Fig.1

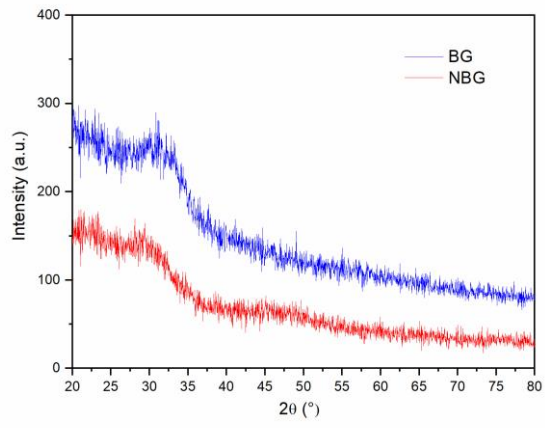


Fig. 2

1  
2  
3  
4  
5  
6  
7  
8  
9  
10  
11  
12  
13  
14  
15  
16  
17  
18  
19  
20  
21  
22  
23  
24  
25  
26  
27  
28  
29  
30  
31  
32  
33  
34  
35  
36  
37  
38  
39  
40  
41  
42  
43  
44  
45  
46  
47  
48  
49  
50  
51  
52  
53  
54  
55  
56  
57  
58  
59  
60  
61  
62  
63  
64  
65

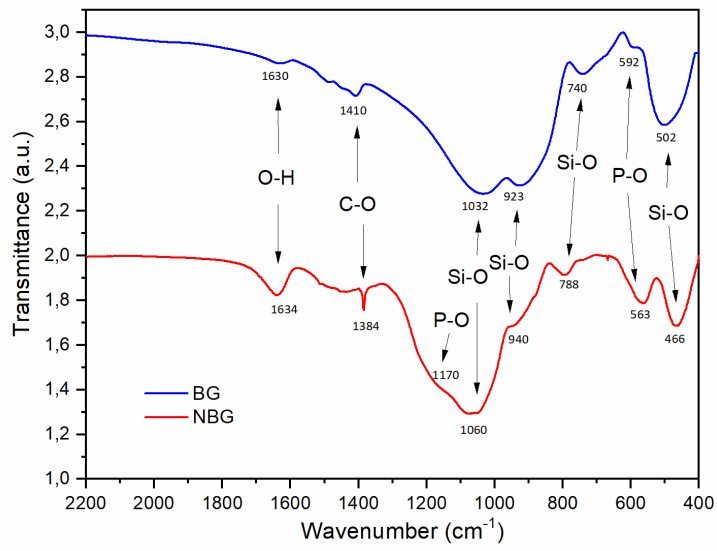


Fig. 3

1  
2  
3  
4  
5  
6  
7  
8  
9  
10  
11  
12  
13  
14  
15  
16  
17  
18  
19  
20  
21  
22  
23  
24  
25  
26  
27  
28  
29  
30  
31  
32  
33  
34  
35  
36  
37  
38  
39  
40  
41  
42  
43  
44  
45  
46  
47  
48  
49  
50  
51  
52  
53  
54  
55  
56  
57  
58  
59  
60  
61  
62  
63  
64  
65

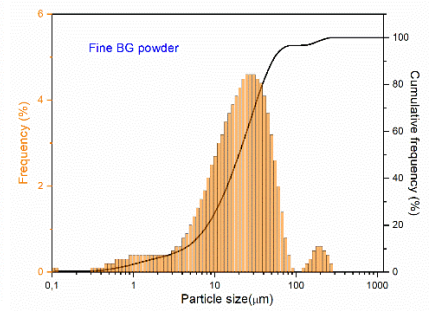
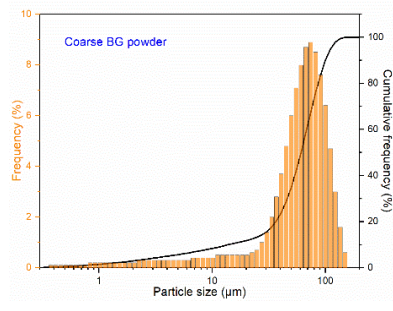
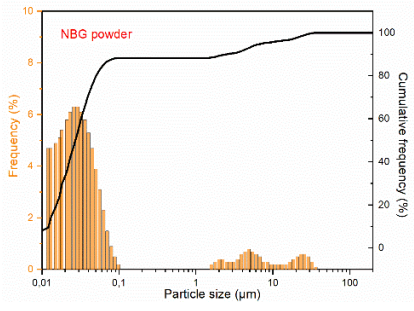
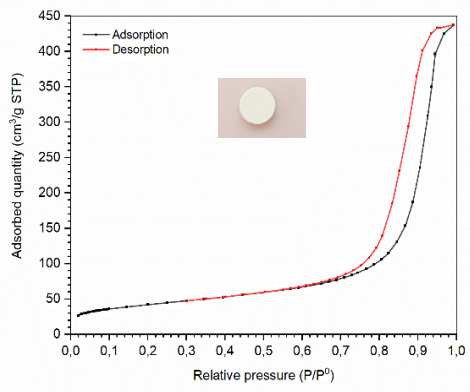
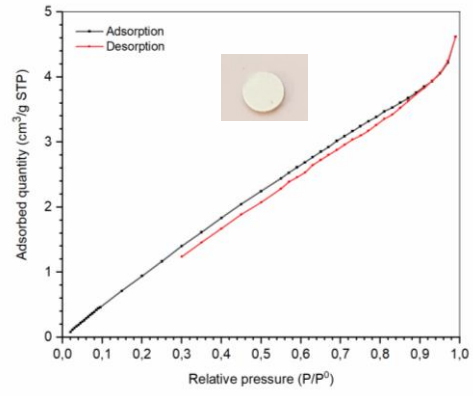


Fig. 4



a



b

Fig. 5

1  
2  
3  
4  
5  
6  
7  
8  
9  
10  
11  
12  
13  
14  
15  
16  
17  
18  
19  
20  
21  
22  
23  
24  
25  
26  
27  
28  
29  
30  
31  
32  
33  
34  
35  
36  
37  
38  
39  
40  
41  
42  
43  
44  
45  
46  
47  
48  
49  
50  
51  
52  
53  
54  
55  
56  
57  
58  
59  
60  
61  
62  
63  
64  
65

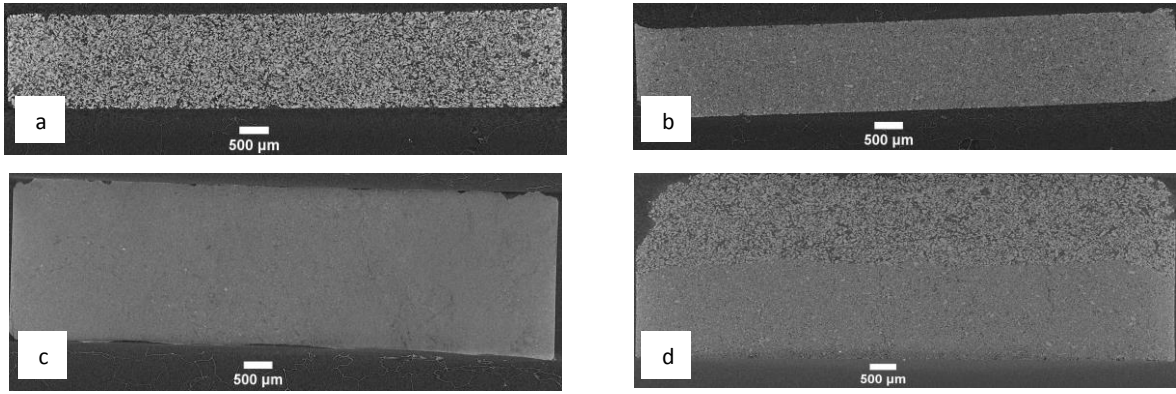
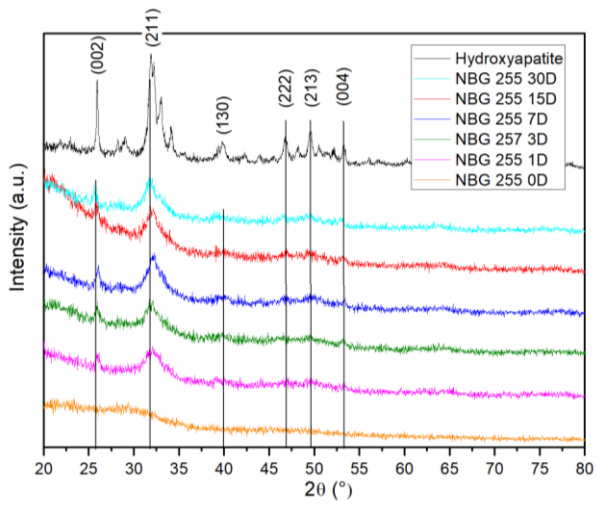


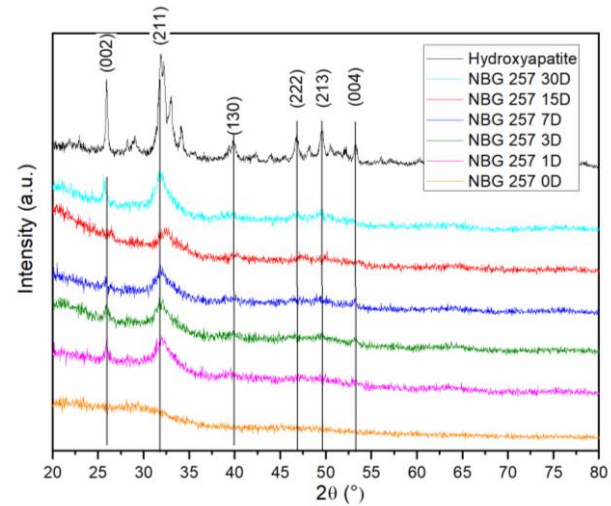
Fig. 6

1  
2  
3  
4  
5  
6  
7  
8  
9  
10  
11  
12  
13  
14  
15  
16  
17  
18  
19  
20  
21  
22  
23  
24  
25  
26  
27  
28  
29  
30  
31  
32  
33  
34  
35  
36  
37  
38  
39  
40  
41  
42  
43  
44  
45  
46  
47  
48  
49  
50  
51  
52  
53  
54  
55  
56  
57  
58  
59  
60  
61  
62  
63  
64  
65

1  
2  
3  
4  
5  
6  
7  
8  
9  
10  
11  
12  
13  
14  
15  
16  
17  
18  
19  
20  
21  
22  
23  
24  
25  
26  
27  
28  
29  
30  
31  
32  
33  
34  
35  
36  
37  
38  
39  
40  
41  
42  
43  
44  
45  
46  
47  
48  
49  
50  
51  
52  
53  
54  
55  
56  
57  
58  
59  
60  
61  
62  
63  
64  
65

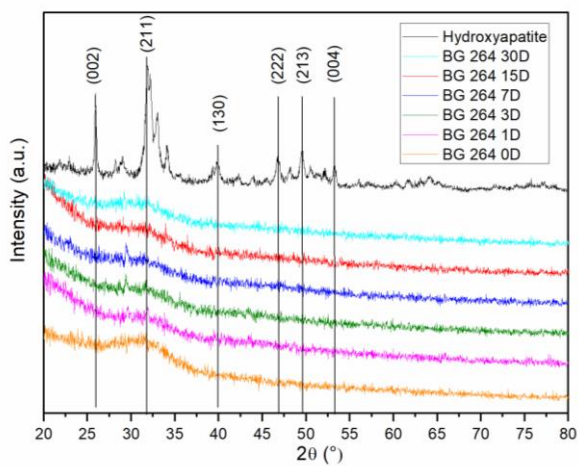


(a)

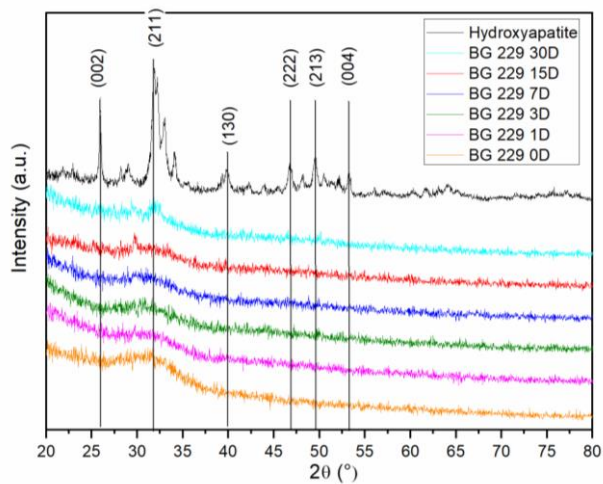


(b)

Fig. 7



(a)



(b)

Fig. 8

1  
2  
3  
4  
5  
6  
7  
8  
9  
10  
11  
12  
13  
14  
15  
16  
17  
18  
19  
20  
21  
22  
23  
24  
25  
26  
27  
28  
29  
30  
31  
32  
33  
34  
35  
36  
37  
38  
39  
40  
41  
42  
43  
44  
45  
46  
47  
48  
49  
50  
51  
52  
53  
54  
55  
56  
57  
58  
59  
60  
61  
62  
63  
64  
65

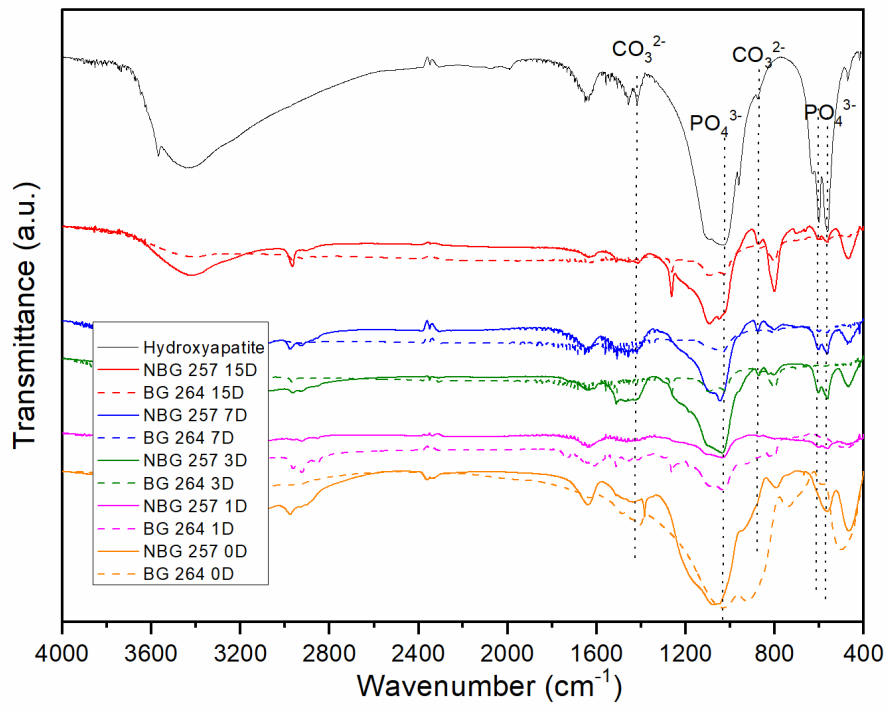
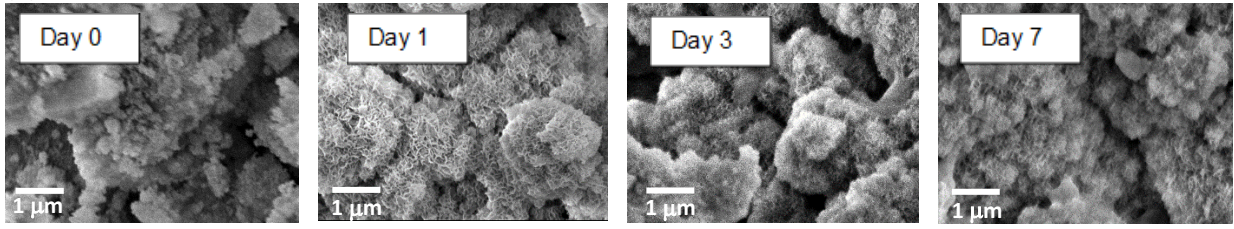


Fig. 9

1  
2  
3  
4  
5  
6  
7  
8  
9  
10  
11  
12  
13  
14  
15  
16  
17  
18  
19  
20  
21  
22  
23  
24  
25  
26  
27  
28  
29  
30  
31  
32  
33  
34  
35  
36  
37  
38  
39  
40  
41  
42  
43  
44  
45  
46  
47  
48  
49  
50  
51  
52  
53  
54  
55  
56  
57  
58  
59  
60  
61  
62  
63  
64  
65

(a) NBG 257



(b) BG 264

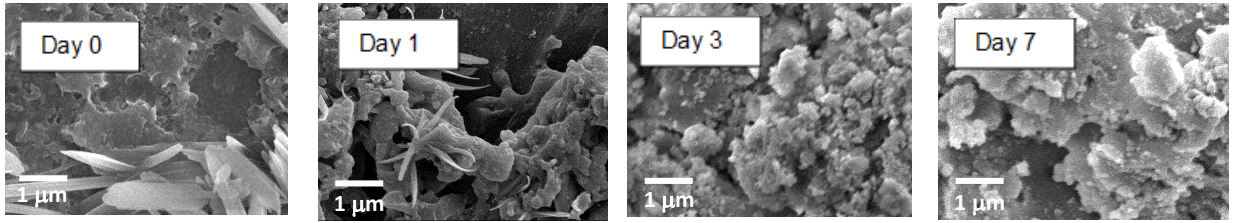
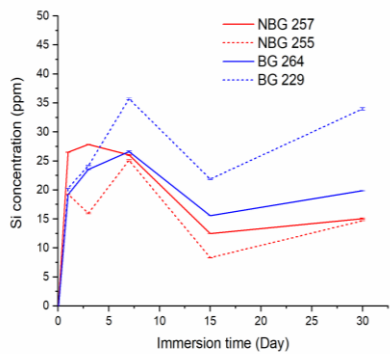


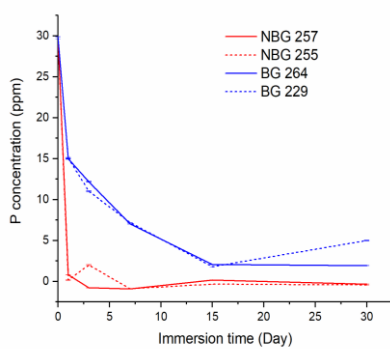
Fig. 10

1  
2  
3  
4  
5  
6  
7  
8  
9  
10  
11  
12  
13  
14  
15  
16  
17  
18  
19  
20  
21  
22  
23  
24  
25  
26  
27  
28  
29  
30  
31  
32  
33  
34  
35  
36  
37  
38  
39  
40  
41  
42  
43  
44  
45  
46  
47  
48  
49  
50  
51  
52  
53  
54  
55  
56  
57  
58  
59  
60  
61  
62  
63  
64  
65

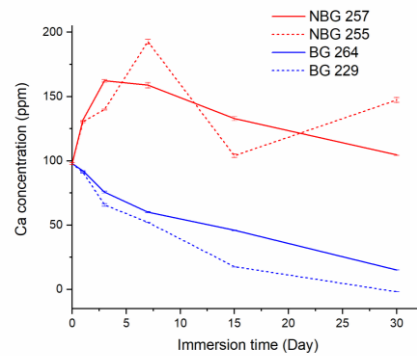
1  
2  
3  
4  
5  
6  
7  
8  
9  
10  
11  
12  
13  
14  
15  
16  
17  
18  
19  
20  
21  
22  
23  
24  
25  
26  
27  
28  
29  
30  
31  
32  
33  
34  
35  
36  
37  
38  
39  
40  
41  
42  
43  
44  
45  
46  
47  
48  
49  
50  
51  
52  
53  
54  
55  
56  
57  
58  
59  
60  
61  
62  
63  
64  
65



(a)



(b)



(c)

Fig. 11

## Supplementary data

### Processing of highly porous bioglass monoliths by hydrothermal hot pressing

B. Degraeve<sup>a</sup>, B. Lefeuvre<sup>a</sup>, N. Rocton<sup>a</sup>, N. Herbert<sup>a</sup>, N. Hamrouni<sup>a</sup>, G. Hauss<sup>b</sup>, A. Largeteau<sup>c</sup>, M. Prakasam<sup>c</sup>, H. Oudadesse<sup>a</sup>, O. Merdrignac-Conanec<sup>a</sup>

<sup>a</sup>Univ Rennes, CNRS, ISCR UMR 6226, 35042, Rennes, France

<sup>b</sup>Univ. Bordeaux, CNRS, PLACAMAT, UMS 3626, F-33600 Pessac, France

<sup>c</sup>Univ. Bordeaux, CNRS, Bordeaux INP, ICMCB, UMR 5026, F-33600 Pessac, France

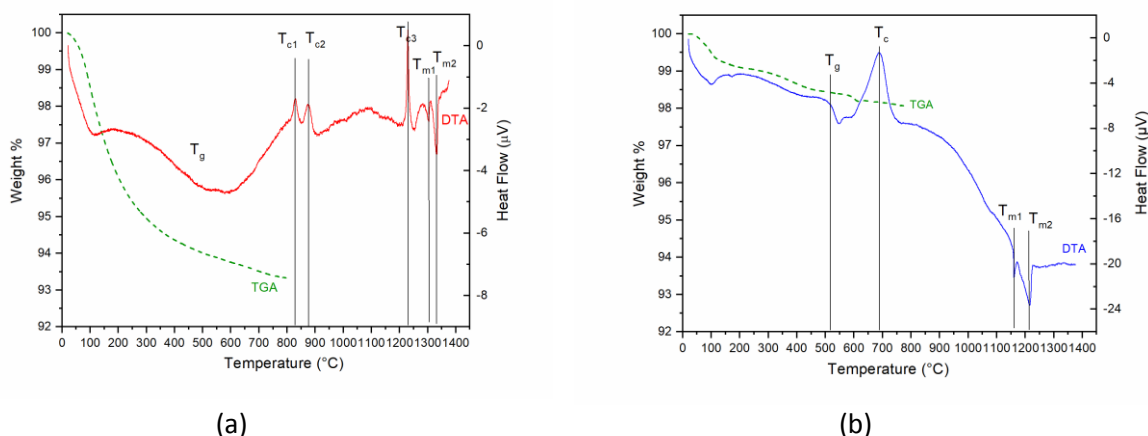


Figure S1. DTA-TGA curves of (a) NBG and (b) BG bioglass powders (heating rate: 10 K.min<sup>-1</sup> in nitrogen)

TGA results show, at 150°C (HyHP sintering temperature), weight losses of 3% and 0.7% for NBG and BG bioglass powders respectively. The DTA curve of NBG powder (Fig. S1a) shows an endothermic effect caused by the glass transition at  $T_g \sim 500^\circ\text{C}$  followed by exothermic crystallisation peaks at  $T_{c1} = 833^\circ\text{C}$ ,  $T_{c2} = 879^\circ\text{C}$  and  $T_{c3} = 1228^\circ\text{C}$  of different silicas and calcium silicate. Finally, two endothermic peaks at  $T_{m1} = 1305^\circ\text{C}$  and  $T_{m2} = 1332^\circ\text{C}$  may be attributed to the melting of two different crystalline phases. The DTA curve of BG powder (Fig. S1b) shows an endothermic effect caused by the glass transition at  $T_g = 530^\circ\text{C}$  followed by an exothermic crystallisation peak at  $T_c = 690^\circ\text{C}$  of sodium calcium silicate and two endothermic peaks at  $T_{m1} = 1160^\circ\text{C}$  and  $T_{m2} = 1218^\circ\text{C}$  attributed to the melting of two different crystalline phases of which sodium calcium silicate. The results are in agreement with those presented in previous works [1-3].

#### References

- [1] E. Dietrich, Synthèse et études physico-chimiques de verres bioactifs denses et poreux. Applications en tant que biomatériaux en sites osseux, PhD Dissertation, Université de Rennes 1 (2008)
- [2] X.V. Bui, Elaboration de biomatériaux verres-substances actives (zolétronate-chitosane). Caractérisations physico-chimiques. Expérimentations "in vitro", PhD Dissertation, Université de Rennes 1 (2011)
- [3] L. Lefebvre, J. Chevalier, L. Gremillard, R. Zenati, G. Thollet, D. Bernache-Assolant, A. Govin, Structural transformations of bioactive glass 45S5 with thermal treatments, *Acta Mater.* 55 (2007) 3305–3313 <https://doi:10.1016/j.actamat.2007.01.029>

Table S1. Density (impregnation method) and open porosity of BG and NBG HyHP sintered monoliths. The density of the sintered samples was calculated from the data obtained by the Archimedes method, according to the European Standard EN623-2 [34].

Sample	Density (g/cm <sup>3</sup> )	Open porosity (%)
NBG 255	0.70 ± 0.01	70.4
NBG 257	0.66 ± 0.01	72.7
BG 264	1.48 ± 0.01	41.5
BG 229	1.45 ± 0.01	43.8